






## Article

# Novel Oxygen- and Curcumin-Laden Ionic Liquid@Silica Nanocapsules for Enhanced Antimicrobial Photodynamic Therapy

Joana Henriques <sup>1</sup>, João Pina <sup>2</sup>, Mara E. M. Braga <sup>1</sup>, Ana M. A. Dias <sup>1</sup>, Patrícia Coimbra <sup>1,\*</sup>  
and Hermínio C. de Sousa <sup>1,\*</sup>

<sup>1</sup> Chemical Process Engineering and Forest Products Research Centre, Department of Chemical Engineering, University of Coimbra, 3030-790 Coimbra, Portugal

<sup>2</sup> Coimbra Chemistry Centre-Institute of Molecular Sciences, Department of Chemistry, University of Coimbra, 3004-535 Coimbra, Portugal

\* Correspondence: patricia@eq.uc.pt (P.C.); hsousa@eq.uc.pt (H.C.d.S.)

**Abstract:** The efficiency of photodynamic therapy is often limited by the scarcity of oxygen at the target site. To address this problem, this work proposes the development of a new nanosystem for antimicrobial photodynamic therapy applications (aPDT) where the natural-origin photosensitizer curcumin (CUR) is immersed in an oxygen-rich environment. Inspired by the perfluorocarbon-based photosensitizer/O<sub>2</sub> nanocarriers reported in the literature, we developed a new type of silica nanocapsule containing curcumin dissolved in three hydrophobic ionic liquids (ILs) with high oxygen dissolving capacities. The nanocapsules (CUR-IL@ncSi), prepared by an original oil-in-water microemulsion/sol-gel method, had a high IL content and exhibited clear capacities to dissolve and release significant amounts of oxygen, as demonstrated by deoxygenation/oxygenation studies. The ability of CUR-IL solutions and of CUR-IL@ncSi to generate singlet oxygen (<sup>1</sup>O<sub>2</sub>) upon irradiation was confirmed by the detection of <sup>1</sup>O<sub>2</sub> phosphorescence at 1275 nm. Furthermore, the enhanced capacities of oxygenated CUR-IL@ncSi suspensions to generate <sup>1</sup>O<sub>2</sub> upon irradiation with blue light were confirmed by an indirect spectrophotometric method. Finally, preliminary microbiological tests using CUR-IL@ncSi incorporated into gelatin films showed the occurrence of antimicrobial effects due to photodynamic inactivation, with their relative efficiencies depending on the specific IL in which curcumin was dissolved. Considering these results, CUR-IL@ncSi has the potential to be used in the future to develop biomedical products with enhanced oxygenation and aPDT capacities.

**Keywords:** silica nanocapsules; curcumin; ionic liquids; oxygen storage/release; photodynamic inactivation



**Citation:** Henriques, J.; Pina, J.; Braga, M.E.M.; Dias, A.M.A.; Coimbra, P.; de Sousa, H.C. Novel Oxygen- and Curcumin-Laden Ionic Liquid@Silica Nanocapsules for Enhanced Antimicrobial Photodynamic Therapy. *Pharmaceutics* **2023**, *15*, 1080. <https://doi.org/10.3390/pharmaceutics15041080>

Academic Editors: Rosemeyre A. Cordeiro and Adérito J. R. Amaral

Received: 24 February 2023  
Revised: 22 March 2023  
Accepted: 23 March 2023  
Published: 28 March 2023



**Copyright:** © 2023 by the authors. Licensee MDPI, Basel, Switzerland. This article is an open access article distributed under the terms and conditions of the Creative Commons Attribution (CC BY) license (<https://creativecommons.org/licenses/by/4.0/>).

## 1. Introduction

Photodynamic therapy (PDT) is a biomedical therapeutic approach that combines three components that alone usually do not elicit a toxic response in biological systems: a photosensitive compound, a light source with a well-defined wavelength, and molecular oxygen (O<sub>2</sub>) [1,2]. PDT is based on the occurrence of a non-thermal photodynamic reaction in which, upon light irradiation with a suitable wavelength, the photosensitizer (PS) is activated, reacts with O<sub>2</sub>, and generates reactive oxygen species (ROS) (through Type I and Type II reactions) that induce a cytotoxic effect on the desired target cells [1–3]. Compared to other cytotoxic therapies, PDT has the major advantage of exhibiting double selectivity: PS can be designed to preferentially accumulate in specific target cells or tissues, and light can be applied exclusively to the specific regions to be treated and for pre-determined treatment periods [1,2]. This spatiotemporal selectivity makes PDT a therapy that has relatively few, non-severe side effects and that may be suitable for repeated applications in situations of recurrence or multiple lesions.

Despite its advantages, PDT has several shortcomings. The typical low chemical stability and hydrophobicity of most PSs are two examples of these limitations [3,4]. Since biological systems are aqueous environments, hydrophobic PSs are prone to aggregate and change their photochemical properties, thus reducing their ROS production efficiency [3,4]. To address these issues, the incorporation of PSs into stable and non-toxic nano-vehicles has been one of the most employed methodologies to enhance PS bioavailability and to improve PDT efficacy [2,3,5]. This general approach can also enable active cellular targeting, which is mostly achieved by chemical or physical surface functionalisation of nanoparticles (NPs) with specific chemical ligands [5–7]. Several recent reviews are available in the literature reporting the use of numerous types of NPs in PDT applications [3–5,8,9], such as inorganic NPs [4], polymeric NPs [8], liposomes [9,10], micelles [11,12], and metal-organic frameworks (MOFs) [7]. Another relevant aspect that may hinder PDT efficiency is oxygen scarcity in pathogenic tissues. To address this issue, PS-loaded NPs with oxygen storage or oxygen generating properties have already been proposed [13]. One example is PS-loaded nanocapsules incorporating perfluorocarbons, a class of fluorinated compounds with high oxygen solubility and capture/release capacities [10,11].

Although most applications of PDT are essentially focused on anticancer therapies, and therefore most PS-loaded NPs have been developed for these purposes, the photodynamic effect has also been explored for the inactivation of microorganisms [14,15], being referred to as antimicrobial photodynamic therapy (aPDT). In this context the use of PS-loaded NPs has also found relevant applications [16], particularly for infected wound management, where light-activated nanoparticles with photodynamic and/or photothermal properties have been combined with polymeric materials to produce antimicrobial multifunctional wound dressings [17,18]. Nevertheless, other biomedical products using this type of antimicrobial nanosystem can be easily envisaged, such as aqueous suspensions, hydrogels, creams/ointments, bioadhesives, bone cements, device coatings, etc.

Considering these potential applications, in this study we present light-responsive silica-based nanocapsules with the ability to generate oxygen singlet in the presence of molecular oxygen and upon irradiation with blue light. These nanosystems consist of a porous and light-transparent silica shell encapsulating different hydrophobic ionic liquids (ILs), in which curcumin, a natural-origin PS, is dissolved. In addition to their curcumin-solubilizing properties, the selected ILs have relatively high oxygen dissolving capacities [19–21], thus enabling the maintenance of high oxygen levels around the PS molecules, which is an indispensable factor for the effectiveness of PDT and aPDT.

Porous silica-based NPs, including silica-based nanocapsules (ncSi), have been extensively tested for the immobilization and/or encapsulation of bioactive substances, PSs, and imaging agents due to a well-known set of favourable properties for these applications such as low toxicity and good biocompatibility, chemical and mechanical stability, transparency, micro/mesoporosity, and a surface chemistry that allows functionalisation/bioconjugation through a series of chemical (and physical) modifications [22,23].

Curcumin is a naturally occurring PS that has been extensively studied for aPDT applications, primarily due to its inherent ability to generate ROS, particularly singlet oxygen, upon exposure to blue light [24]. Curcumin also exhibits several other important and well-known biological properties, such as anticancer and anti-inflammatory activities [25]. However, curcumin is a highly hydrophobic compound with a poor solubility and stability in aqueous solutions, which severely limits its straightforward use in most biological applications [25]. Furthermore, and due to self-aggregation in aqueous systems, curcumin in water usually exhibits a very low singlet oxygen sensitization quantum yield [26]. To improve its stability and bioavailability as well as its phototoxicity, curcumin has been encapsulated/immobilized in several NPs and other nanoformulations [6,25,27,28] using conventional processing oils/solvents and non-conventional hydrophobic solvents, such as deep eutectic solvents or ionic liquids [29,30].

Due to their chemical and physical properties, as well as their easy “tunability” features, it is known that a large number of ILs can be “designed” and synthesized in order

to solubilize either some specific or a wide range of solutes. In addition to this, ILs may also have other favourable properties as processing solvents for a wide range of applications, including in the pharmaceutical and biomedical fields (such as their very low, or non-existent volatilities, or their potentially high chemical and thermal stabilities) [31,32]. Additionally, due to some of their specific chemical/physical properties, it is possible to find some particular ILs that can absorb significant amounts of different gases, including respiratory gases (such as CO<sub>2</sub> and O<sub>2</sub>). In fact, several ILs (alone or in combination with other substances/materials) have been extensively studied and tested for a variety of different applications involving the capture, storage, transport, and/or release of gases, especially CO<sub>2</sub> [19,33]. Some ILs containing (per)fluorinated anions (more common) or cations (less common) can exhibit particularly high O<sub>2</sub> solubilization capacities and have been proposed as low volatility alternatives to the typical perfluorocarbons that have been studied for oxygen carrying applications in the medical field [19]. Therefore, herein we explored the use of three different hydrophobic ILs as hydrophobic solvents able to solubilize curcumin and to simultaneously provide local high O<sub>2</sub> concentrations around curcumin. The selected ILs represent three different IL families/types—pyrrolidinium, imidazolium, and phosphonium, although all of them contain the same perfluorinated bis (trifluoromethylsulfonyl) imide anion: 1-butyl-1-methylpyrrolidinium bis(trifluoromethylsulfonyl)imide [BMPYRR][NTf<sub>2</sub>]; 1-octyl-3-methylimidazolium bis(trifluoromethylsulfonyl)imide [OMIM][NTf<sub>2</sub>]; and trihexyltetradecylphosphonium bis(trifluoromethylsulfonyl)imide [P<sub>6,6,6,14</sub>][NTf<sub>2</sub>].

In the last decade, the micro/nanoencapsulation of ILs in inorganic or polymeric porous/permeable shells has been proposed as a strategy to overcome some capture/release problems related to the kinetic limitations usually imposed by the typically poor mass transport properties of ILs in many practical applications [33]. So far, this strategy has been explored in the fields of chemical synthesis and biocatalysts, removal of some water pollutants, energy storage, and, in particular, for CO<sub>2</sub> capture and separation applications. In contrast, the potential applications of encapsulated ILs in the pharmaceutical and biomedical fields remain practically unexplored [31,33]. In fact, and to the best of our knowledge, the encapsulation of liquid solutions containing a PS and an IL for PDT or aPDT applications has never been reported in the literature, which highlights the innovative nature of the strategies/materials reported in this work.

## 2. Materials and Methods

### 2.1. Materials

Ionic Liquids (ILs) 1-butyl-1-methylpyrrolidinium bis(trifluoromethylsulfonyl)imide ([BMPYRR][NTf<sub>2</sub>], 99% purity), 1-octyl-3-methylimidazolium bis(trifluoromethylsulfonyl)imide ([OMIM][NTf<sub>2</sub>], 99% purity), and trihexyltetradecylphosphonium bis(trifluoromethylsulfonyl)imide ([P<sub>6,6,6,14</sub>][NTf<sub>2</sub>], >98% purity) were acquired from IoLiTec GmbH, Heilbronn, Germany. Tetraethyl orthosilicate (TEOS, >99% purity), co-surfactant/co-precursor (1H, 1H, 2H, 2H-perfluorooctyl) triethoxysilane (TEOFSilane, 98% purity), polyethylene glycol sorbitan monooleate (Tween<sup>®</sup>80), 4-(2-hydroxyethyl)-1-piperazineethanesulfonic acid (HEPES, >99.5% purity), curcumin (extract from *Curcuma longa*, ~80% purity; the last 20% contain other curcuminoids), gelatin (from porcine skin, type A, bloom 300), and phosphate buffered saline tablets (PBS) were purchased from Sigma Aldrich, Barcelona, Spain. 1,3-diphenylisobenzofuran (DPBF, >95% purity) was purchase from TCI Europe N.V., Zwijndrecht, Belgium. *Lactobacillus rhamnosus* (DSMZ 20,021) was obtained from DSMZ (German Collection of Microorganisms and Cell Cultures GmbH, Braunschweig, Germany) and Man, Rogosa and Sharpe (MRS) broth was provided by Scharlab, Barcelona, Spain. All other used chemicals were of analytical grade.

### 2.2. Synthesis of CUR-IL@ncSi Nanocapsules

Curcumin (CUR) and IL-loaded silica nanocapsules were prepared by a combined oil-in-water microemulsion/sol-gel method using an original and dual-purpose co-surfactant/silica co-precursor agent.

Curcumin was dissolved in the tested ILs (2 mg of curcumin per gram of IL) at room temperature. Surfactants Tween<sup>®</sup>80 and TEOFSilane (in a 3:1 mol:mol relative composition and in a 10:1 mol:mol ratio concerning the amount of IL) were dissolved in Milli-Q water (48 mL). Then, 0.5 mL of each curcumin/IL solution was added to the surfactants solution and the mixture was emulsified for 10 min using an ultrasound processor (Sonics VCX750, 750 W, 20 kHz, Sonics & Materials Inc., Newtown, CT, USA) operating at 30% amplitude in a 1 s pulse on/off mode. Each CUR-IL/water emulsion obtained was acidified with 0.5 M HCl to pH ~2.1, to hydrolyse the co-surfactant/silica co-precursor TEOFSilane, and left under magnetic stirring for 45 min. At the same time, 0.3 mL of TEOS was added to 10 mL of HCl acidified Milli-Q water (pH ~2.1) and hydrolysed under vigorous magnetic stirring (500 rpm) for 30 min. Subsequently, the hydrolysed TEOS solution was added to the CUR-IL/water emulsion, followed by the addition of 8 mL of a 0.1 M HEPES buffer solution. Finally, the pH of the emulsion was measured and adjusted to pH 7.3–7.5 with 0.5 M NaOH solution. The formation of the silica shell around CUR-IL/water emulsion micelles took place for 24 h, at room temperature, and under magnetic stirring (800 rpm). The formed CUR-IL-loaded silica nanocapsules (CUR-IL@ncSi) were isolated by centrifugation (1126 rcf, 5 min), washed twice with distilled water, frozen, and freeze-dried. In addition, nanocapsules containing only the tested ILs (IL@ncSi) were prepared (as controls) using the same procedures described above. A schematic representation of this procedure is shown in Figure 1.

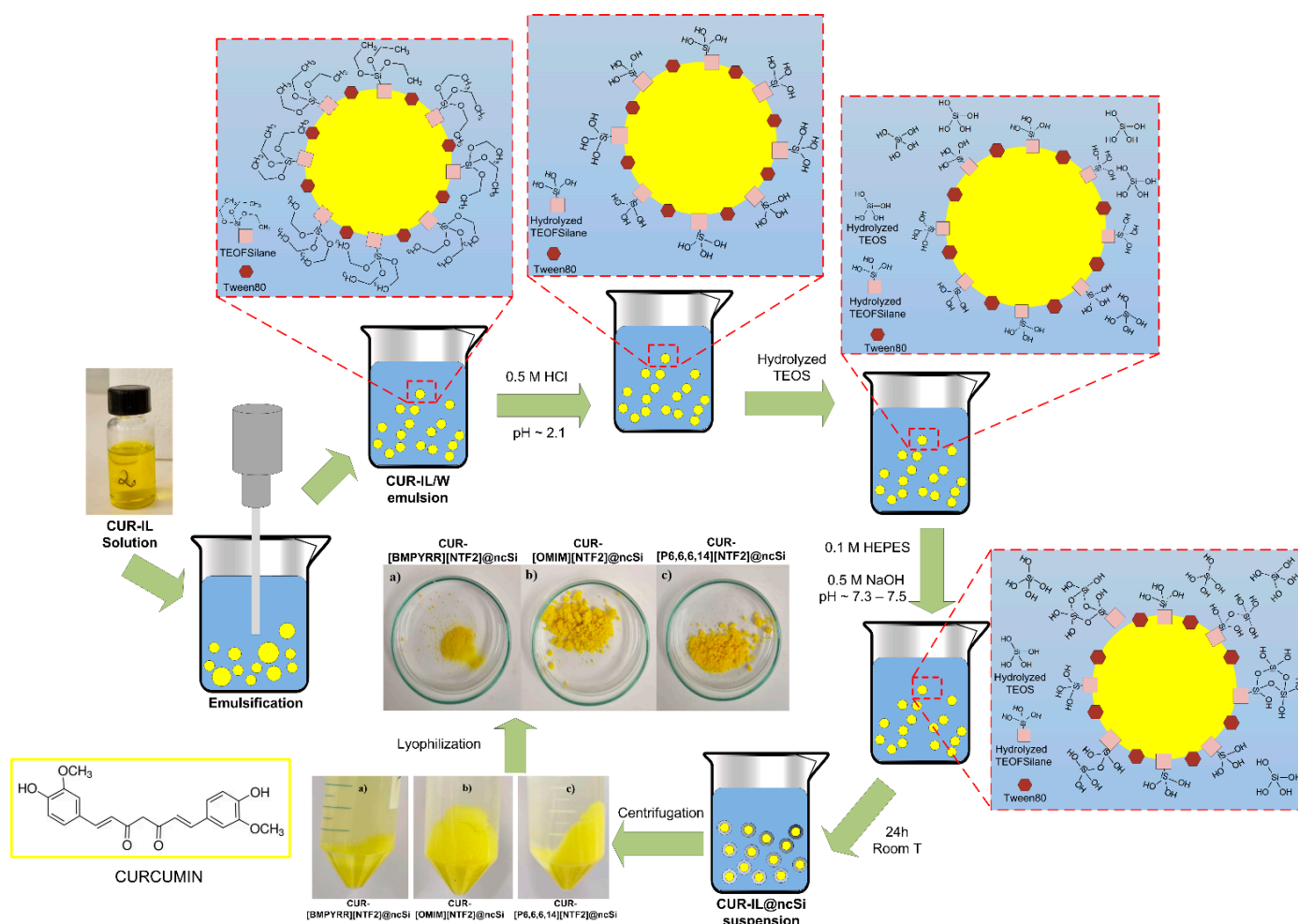


**Figure 1.** Schematic representation of the nanocapsule preparation process. Inserted pictures: (a) CUR-[BMPYRR][NTF<sub>2</sub>]@ncSi; (b) CUR-[OMIM][NTF<sub>2</sub>]@ncSi; and (c) CUR-[P<sub>6,6,6,14</sub>][NTF<sub>2</sub>]@ncSi.

### 2.3. Nanocapsules Characterization

The silica and IL contents of the prepared CUR-IL@ncSi nanocapsules were estimated by thermogravimetric analysis with a simultaneous TGA/DSC analyzer (SDT) Q600 from TA Instruments (New Castle, DE, USA). In brief, 5–10 mg samples were heated from room temperature up to 600 °C, under a nitrogen flux, at a constant heating rate of 10 °C/min. The mass remaining at 600 °C was assumed to correspond to the amount of silica present in the nanocapsules. In addition, the relative amount of ILs in the prepared ncSi were also determined by elemental analysis (CHNS-O analyzer, model EA1108, Fisons Instruments, Glasgow, UK), by quantifying the elemental sulfur present in the samples due to the [NTf<sub>2</sub>] anion.

The particle sizes of the CUR-IL/water emulsions and of the resulting CUR-IL@ncSi nanocapsules were analyzed by Dynamic Light Scattering (DLS) in a Zetasizer Nano ZS (Malvern Instruments, Malvern, UK).

The morphology of the CUR-IL@ncSi nanocapsules was assessed microscopically by SEM/STEM (FE-SEM Zeiss Merlin Gemini 2, CarlZeiss AG, Oberkochen, Germany).

### 2.4. Oxygen Loading/Release Experiments

The oxygen loading/release capacity of CUR-IL@ncSi nanocapsules was assessed using a protocol and experimental setup similar to that described by Lambert et al. [34]. First, a glass vial containing 30 mL of deionized water, under magnetic stirring (100 rpm) and with an immersed oxygen probe (SZ10T Consort Dissolved Oxygen Electrode), was bubbled with nitrogen (2 bar) until the oxygen concentration in the water reached a constant value, close to zero. At the same time, a suspension of CUR-IL@ncSi nanocapsules (40 mL) was oxygenated by bubbling oxygen (2 bar) for 20 min under magnetic stirring (100 rpm). The concentration of nanocapsules in the suspension corresponded to an IL to water ratio of approximately 1:80 *v/v*. Immediately after closing the O<sub>2</sub> flow, a sample of 10 mL of the CUR-IL@ncSi nanocapsule suspension was taken with the help of a syringe and injected into the vial containing the degassed water, which was immediately isolated from the surrounding atmosphere with Teflon sealing tape. The evolution of the oxygen concentration in the release medium over time was then followed and recorded using an oxygen probe connected to a Consort C3010—Multi-Parameter analyzer (Consort, Turnhout, Belgium). The temperature was kept constant (25 °C) during both loading/release experiments, by placing the vials in glass thermal jackets connected to a thermostatically controlled bath (model CC-K6, Huber, Offenburg, Germany). For comparison, the oxygen loading/release capacities of the corresponding CUR-IL/water emulsions (IL:water ~1:96 *v/v*) were also studied. Oxygenated deionized water was used as a control. All experiments were performed in triplicate using samples (nanocapsules and emulsions) prepared less than one week before.

### 2.5. Singlet Oxygen Generation Experiments

The curcumin capacity to generate singlet oxygen (<sup>1</sup>O<sub>2</sub>) when dissolved in the studied ILs was determined by the direct measurement of phosphorescence at 1275 nm, after sample irradiation with a 355 nm Nd:YAG laser. The experimental setup is described elsewhere [35]. The samples analyzed were: (i) air-saturated curcumin/IL solutions (1 mg/g<sub>IL</sub>); and (ii) air-saturated aqueous suspensions of CUR-IL@ncSi nanocapsules (~12 mg/mL). Singlet oxygen lifetimes were determined by fitting the experimental data (phosphorescence intensity at 1275 nm vs. time) with a first-order exponential model.

The capacity of CUR-IL@ncSi nanocapsules to release singlet oxygen into its aqueous surrounding when irradiated with blue light was determined by an indirect method using the chemical probe 1,3-diphenylisobenzofuran (DPBF) [36]. Samples were prepared immediately before use by mixing, in quartz cuvettes, 200 µL of DPBF fresh stock solution in ethanol (1 mM) with 1.8 mL of an aqueous CUR-IL@ncSi nanocapsule suspension (~6.6 mg/mL). The suspensions were kept under magnetic stirring in the dark for one minute. The cuvettes were then transferred to a 60 mm integrating sphere (Jasco, model

ISV-722) in a JASCO 650 UV-VIS spectrophotometer (JASCO Corporation, Tokyo, Japan) and their initial absorbance spectra were recorded. The samples were then irradiated with a blue light (450 nm blue light LED Lamp, 5 W) placed at a distance of 82 cm, and their spectra were recorded after each 10 s of light irradiation. Spectra were also obtained for samples subjected to the same procedures but without blue light exposure (controls). In addition, and following the same procedures, the spectra of oxygenated samples (i.e., nanocapsule suspensions previously bubbled with pure O<sub>2</sub> for 15 min) were recorded (in this case, the cuvettes were adequately sealed with airtight stoppers immediately after DPBF addition). Finally, for comparison purposes, and again following the same experimental procedures, the spectra of DPBF in the presence of solubilized curcumin (90:10 (v/v) water:ethanol) were also recorded.

The experiments were performed in triplicate for each type of sample tested. For each run, the absorbance intensities of DPBF at 416 nm were normalized with the absorbance of the non-irradiated sample ( $A_t/A_0$ , where  $A_0$  is the absorbance of the non-irradiated sample) and plotted against irradiation time.

### 2.6. Antimicrobial Photodynamic Activity

The antimicrobial activity of the prepared nanocapsules was evaluated for freeze-dried CUR-IL@ncSi nanocapsules immobilized in a gelatin film. In brief, gelatin was dissolved in sterilized PBS (0.01 M, pH 7.4, 0.0027 M KCl, 0.137 M NaCl) at a concentration of 10% w/v, at 50 °C. Nanocapsules were then added to the gelatin solution (at the amount of 20% of the gelatin mass, 20 mg of CUR-IL@ncSi per mL of gelatin solution), and the resulting suspension was vortex-homogenized, cast in plastic Petri dishes (5 mL of the resulting viscous suspension), and left to dry overnight in a ventilated oven at 25 °C. The formed films (~150 µm thick) were cut into 1 cm diameter disks and laid at the bottom of the wells of a 48-wells cell culture plate. In addition to gelatin films containing CUR-IL@ncSi nanocapsules, other films were prepared by the same procedures to be used as controls: (i) films containing only gelatin; and (ii) films containing IL@ncSi nanocapsules (without curcumin).

*Lactobacillus rhamnosus* (*L. rhamnosus*) was used as a model for Gram-positive bacteria. *L. rhamnosus* were inoculated into 40 mL of MRS culture medium and grown overnight at 35 °C in an orbital shaker incubator. The resulting culture with a cell concentration of ~10<sup>8</sup> CFU/mL was isolated, washed with PBS, and diluted with PBS to obtain a suspension with a cellular concentration of ~10<sup>5</sup> CFU/mL. Then, 1 mL of this suspension was added to each well of the 48-wells cell culture plate already containing the gelatin discs to be tested. Wells without gelatin discs were used as controls. The plate was left to rest in the dark for 30 min and then irradiated with a blue light (450 nm blue light LED Lamp, 5 W), placed 20 cm above, for up to 2 h. At each irradiation time point (0, 1, and 2 h), 10 µL of cell suspensions were removed from each well and added to the wells of a 96-wells cell culture plate. After, 90 µL of MRS broth was added to each well and the 96-wells plate was placed in a Synergy HTX multi-mode microplate reader (BioTeck, Winooski, VT, USA), at 35 °C, where the absorbance of the samples at 600 nm was measured automatically over 24 h. Experiments were performed in triplicate for all systems/controls tested.

### 2.7. Statistical Analysis

Data are expressed as mean ± standard deviation. Comparisons between multiple groups were made with an analysis of variance (ANOVA) followed by a post-hoc Tukey test. Comparisons between two groups were made using a Student's *t*-test. A *p*-value of <0.05 was considered to be statistically significant.

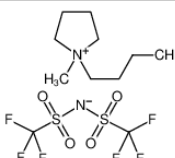
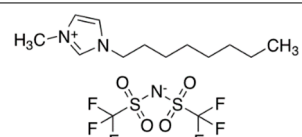
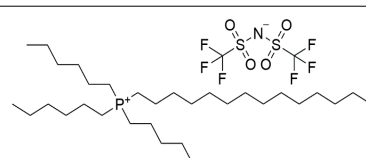
## 3. Results and Discussion

This work aims to develop novel, more efficient, and stable silica-shell nanocapsules that can be foreseen as light-responsive nanosystems for aPDT in biomedical applications. These nanocapsules contain a natural photosensitizer (curcumin) in their core, which

is dissolved in hydrophobic ILs with relatively high oxygen dissolving capacities. Their liquid cores, together with their transparent and porous silica shells (which provide stability, transparency, and good oxygen/ROS diffusivity) offer essential advantageous conditions for the occurrence of more efficient photodynamic reactions when exposed to light.

The three hydrophobic ILs tested ([BMPYRR][NTf<sub>2</sub>], [OMIM][NTf<sub>2</sub>], and [P<sub>6,6,6,14</sub>][NTf<sub>2</sub>], represented in Table 1), were selected from a larger group of commercially available ILs, with the main criteria being their high water immiscibility (high hydrophobicity) and their high O<sub>2</sub> solubility capacities (supported by the literature data). In addition, three of the most relevant IL families are represented in this selection: imidazolium-, phosphonium-, and pyrrolidinium-types of ILs. All these three cations, especially [P<sub>6,6,6,14</sub>] and [OMIM], have long alkyl chains, which are known to promote high hydrophobicity [37–39] and O<sub>2</sub> solubility [20,21]. Furthermore, all these ILs contain the perfluorinated anion [NTf<sub>2</sub>], which is reported to be one of the most hydrophobic and O<sub>2</sub>-phylic anions [37,38]. An additional criterion for the selection of these ILs was their ability to dissolve relatively high amounts of curcumin (it was observed that curcumin was readily soluble in the three selected ILs and remained stable and active in solution for at least three months, when protected from light).

**Table 1.** Name, chemical structure, solubility in water, and oxygen solubility of the three ILs used in this work.

IL	Name	Chemical Structure	Solubility in Water (mol/mol)	O <sub>2</sub> Solubility [mM]
[BMPYRR][NTf <sub>2</sub> ]	1-Butyl-1-methylpyrrolidinium bis(trifluoromethylsulfonyl)imide		$2.38 \times 10^{-4}$ (25 °C) [38]	$9.1 \pm 0.9$ (25 °C, 1 atm O <sub>2</sub> ) [40]
[OMIM][NTf <sub>2</sub> ]	1-octyl-3-methylimidazolium bis(trifluoromethylsulfonyl)imide		$3.4 \times 10^{-5}$ (25 °C) [37]	$8.3 \pm 0.8$ (25 °C, 1 atm O <sub>2</sub> ) [41]
[P <sub>6,6,6,14</sub> ][NTf <sub>2</sub> ]	trihexyltetradecylphosphonium bis(trifluoromethylsulfonyl)imide		Not available	$6.0 \pm 0.5$ (35 °C, 1 atm O <sub>2</sub> ) [42]

Nanocapsules were prepared using a combined oil-in-water microemulsion and sol-gel method developed and optimized by our research group and schematized in Figure 1. This method involves the emulsification of a CUR-IL solution in a continuous water phase containing a surfactant (Tween<sup>®</sup>80) and a co-surfactant/co-precursor (TEOFSilane). The latter has a highly hydrophobic perfluorinated C6 tail and a triethoxysilane head which, after hydrolysis, will play two different roles: as a co-surfactant, to stabilize CUR/IL micelles; and as a silica co-precursor, acting as an anchor point for condensation of water-soluble hydrolyzed TEOS around the CUR/IL emulsion droplets, thus leading to mechanically stable capsules. As such, a porous silica shell begins to form in the CUR-IL/water interface and the emulsion is converted to a nanocapsule suspension. The hydrolysis/condensation rates of the silica co-precursors (TEOS and TEOFSilane), as well as the resulting shell thickness/porosity and nanocapsules agglomeration/aggregation behavior are essentially controlled by the addition of the HEPES solution and by pH manipulation of the aqueous continuous phase of the CUR-IL/water emulsion. In this work, other experimental variables that can also affect the properties of the nanocapsules (reaction time, temperature, relative compositions (Tween<sup>®</sup>80:TEOFSilane, water, TEOS), stirring conditions, etc.) were

maintained in all the experiments. On the other hand, the nanocapsules' size and size distributions depend mainly on the initial emulsion droplet size (and droplet size distributions), which ultimately result from the chemical properties of the substances involved (IL, water, Tween<sup>®</sup>80, TEOFSilane), from their relative proportions, and from the emulsification conditions employed (e.g., temperature; emulsification method and specific operational conditions; energy provided vs. emulsification time, etc.).

### 3.1. Nanocapsules Characterization

The morphology of CUR-[BMPYRR][NTf<sub>2</sub>]<sup>-</sup>@ncSi nanocapsules can be observed in Figure 2. SEM images show submicron particles with a broad size range. Fragments/empty capsules of larger size can also be observed, probably due to disintegration during their synthesis/processing or sample manipulation. Weiss et al. (2014) observed similar features in IL-containing silica capsules, also prepared by an oil-in-water emulsion/sol-gel method [43]. DLS results confirmed these observations, revealing a size distribution with two main broad size ranges (~100–200 nm, and ~600–1100 nm, Figure S1 in supplementary materials). Similar size distributions were found for CUR-[OMIM][NTf<sub>2</sub>]<sup>-</sup>@ncSi and CUR-[P<sub>6,6,6,14</sub>][NTf<sub>2</sub>]<sup>-</sup>@ncSi, i.e., broader distributions, with peaks centered around 60–100 nm and 350–550 nm, for CUR-[OMIM][NTf<sub>2</sub>]<sup>-</sup>@ncSi (Figure S2), and 200–600 nm, for CUR-[P<sub>6,6,6,14</sub>][NTf<sub>2</sub>]<sup>-</sup>@ncSi (Figure S3). These features are in good agreement with the results obtained for the corresponding emulsion droplet size distributions, which presented broad mono- or bimodal droplet size distributions, with average hydrodynamic sizes between 15–70 nm and 280–350 nm (see Table S1 and Figures S4–S6 in supplementary material).

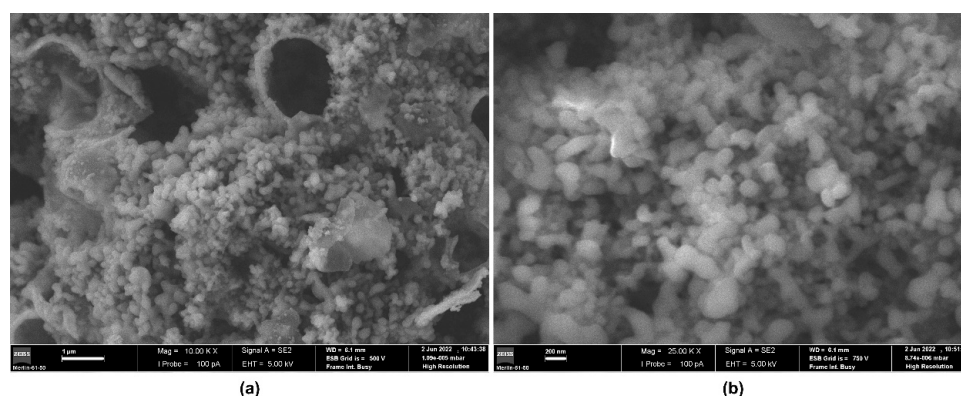


**Figure 2.** SEM images of freeze-dried CUR-[BMPYRR][NTf<sub>2</sub>]<sup>-</sup>@ncSi. Scale Bars: (a) 1 μm; and (b) 200 nm.

STEM analysis (Figure 3) did not allow us to clearly prove the capsular features of the prepared nanocapsules, but the obtained STEM micrographs have confirmed their particle size ranges, namely for the smaller particle sizes in bimodal distributions.

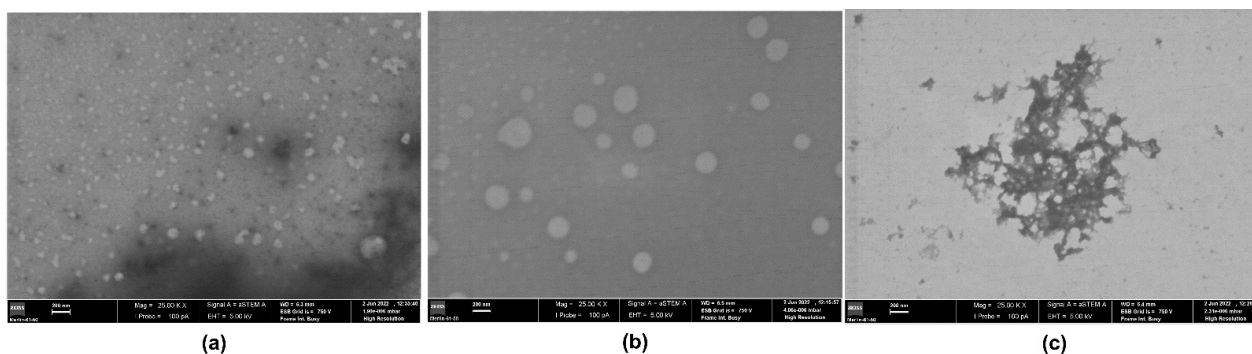


**Figure 3.** STEM images of: (a) CUR-[BMPYRR][NTf<sub>2</sub>]<sup>-</sup>@ncSi; (b) CUR-[OMIM][NTf<sub>2</sub>]<sup>-</sup>@ncSi; and (c) CUR-[P<sub>6,6,6,14</sub>][NTf<sub>2</sub>]<sup>-</sup>@ncSi. Scale bar: 200 nm.



The relative composition of the prepared nanocapsules was estimated by elemental analysis (EA) and thermogravimetric analysis (TGA) (Table 2). EA results (which quantify only the incorporated amounts of ILs) show that CUR-[OMIM][NTf<sub>2</sub>]<sub>@ncSi</sub> and CUR-[P<sub>6,6,6,14</sub>][NTf<sub>2</sub>]<sub>@ncSi</sub> nanocapsules have a very high IL content, about 83.6% and 94.4% *w/w*, respectively, while CUR-[BMPYRR][NTf<sub>2</sub>]<sub>@ncSi</sub> has a substantially lower IL content (35.7% *w/w*). TGA results follow the same general trend although different relative composition values were obtained since the TGA method (gravimetric) does not consider the specific relative amounts of the different organic species present in the samples (i.e., ILs, TEOFSilane, Tween<sup>®</sup>80, and CUR).

**Table 2.** Amount of IL (% *w/w*) incorporated into NCs determined by TGA and by EA.

NC	TGA	EA
CUR-[BMPYRR][NTf <sub>2</sub> ] <sub>@ncSi</sub>	64.4 ± 11.4	35.7 ± 1.6
CUR-[OMIM][NTf <sub>2</sub> ] <sub>@ncSi</sub>	94.0 ± 1.2	83.6 ± 1.5
CUR-[P <sub>6,6,6,14</sub> ][NTf <sub>2</sub> ] <sub>@ncSi</sub>	94.8 ± 2.2	94.4 ± 1.1

The different IL contents can be explained by the corresponding ILs' solubilities in water ([BMPYRR][NTf<sub>2</sub>] > [OMIM][NTf<sub>2</sub>] > [P<sub>6,6,6,14</sub>][NTf<sub>2</sub>]), which determine the propensity of IL to leach into to the water continuous phase during nanocapsules synthesis, processing, and storage in aqueous media. In fact, the solubility of [BMPYRR][NTf<sub>2</sub>] in water is one order of magnitude higher than that of [OMIM][NTf<sub>2</sub>] (see Table 1). As for [P<sub>6,6,6,14</sub>][NTf<sub>2</sub>], although its experimental solubility in water is not available in the literature, it is expected to be the lowest of the three ILs, considering the high hydrophobicity of the [P<sub>6,6,6,14</sub>] cation (derived from its long alkyl chains) and the very low solubility of water in [P<sub>6,6,6,14</sub>][NTf<sub>2</sub>], as reported by Freire et al. (2008) [39].

### 3.2. Nanocapsules Oxygen Loading and Release Capacity

The capacity of the nanocapsules to load and release oxygen was evaluated by analyzing the evolution of the oxygen concentration in deoxygenated water after the addition of (i) an oxygenated CUR-IL<sub>@ncSi</sub> suspension sample; (ii) an oxygenated IL/water emulsion sample; and (iii) an oxygenated water sample (control). As can be seen in Figure 4, the moment each oxygenated sample is introduced the O<sub>2</sub> concentration begins to rise, reaches a maximum, and then declines, converging to a plateau (~3–4 ppm). Since the experiment is performed in a closed flask, where the headspace above the liquid is also initially deoxygenated, the oxygen that is released and dissolved in the water phase will diffuse into the headspace above, until the O<sub>2</sub> concentration in the liquid and gas phases reaches equilibrium. This explains the descending segments of the curves. For the water control, the maximum O<sub>2</sub> concentration (5.4 ppm) was reached after 2 min and 30 s. This time interval can essentially be attributed to the response time of the oxygen sensor since the homogenization and dilution of the two water fractions should be almost instantaneous.

The maximum O<sub>2</sub> concentrations achieved for the studied samples ranged from 7.7 to 8.4 ppm, for nanocapsule suspensions, and 6.7 to 7.6 ppm, for IL/water emulsions. The time to reach the maximum O<sub>2</sub> concentration ranged between 2 and 3 min, for nanocapsule suspensions, and 3 and 5 min for IL/water emulsions. These results clearly show that the maximum concentrations of dissolved O<sub>2</sub> that were observed for the nanocapsule suspensions and the CUR-IL/water emulsions are always higher than the maximum concentrations obtained for the oxygenated water (control), which proves the capacities of these ILs to store and, subsequently, to release O<sub>2</sub> to the water phase, either encapsulated in silica nanocapsules or as the disperse phase of IL/water emulsions. This reflects the higher capacity of ILs to dissolve oxygen in comparison to water (about 5 to 7 times higher, considering the values presented in Table 1 and the solubility of oxygen in pure water (1.22 mM, at 25 °C and 1 atm of O<sub>2</sub> [44])).

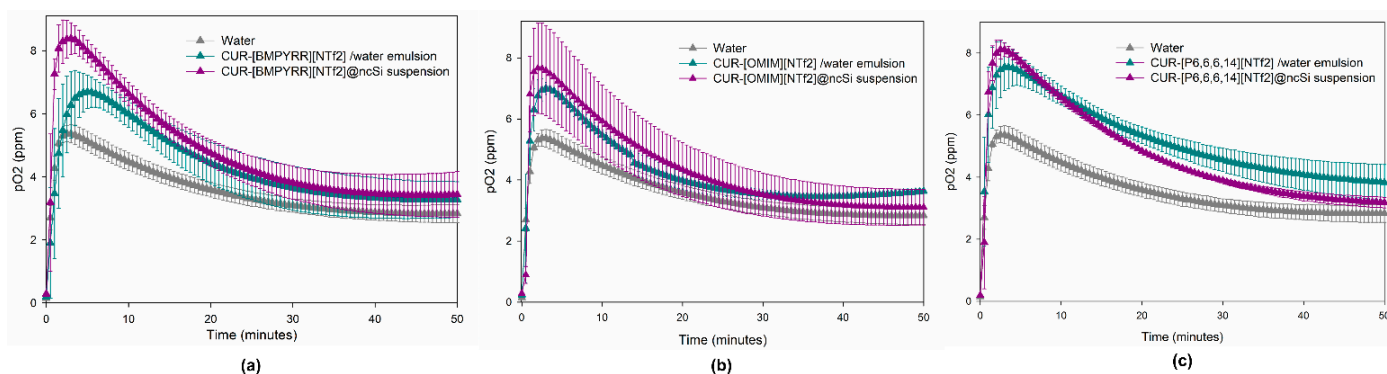


**Figure 4.** Evolution of the oxygen concentration in deoxygenated water after the addition of: (i) oxygenated CUR-IL@ncSi suspension samples; (ii) oxygenated IL/water emulsion samples; and (iii) oxygenated water samples (control). (a) [BMPYRR][NTf<sub>2</sub>]; (b) [OMIM][NTf<sub>2</sub>]; and (c) [P<sub>6,6,6,14</sub>][NTf<sub>2</sub>].

For the same IL, and compared to CUR-IL/water emulsions, nanocapsule suspensions always lead to a higher maximum pO<sub>2</sub> value and a shorter time to reach this value (Table S2, supplementary material). This was not expected since the presence of a silica shell in nanocapsules should impose an additional barrier to mass transfer. Therefore, these results are probably due to the different IL:water (*v/v*) ratios that were employed for CUR-IL@ncSi (1:80) and for CUR-IL/water emulsions (1:96), which result in the dissolution of higher total amounts of O<sub>2</sub> in nanocapsule suspensions than in emulsions, thus leading to enhanced initial O<sub>2</sub> mass transfer gradients in the former. Indeed, for the same IL, the calculated overall volumetric mass transfer coefficients ( $K_L a$ ) for CUR-IL@ncSi were always higher than the corresponding coefficients for the CUR-IL/water emulsions (Table S2, supplemental materials), indicating that O<sub>2</sub> transfer rates are favored when using nanocapsules. This is true even for the case of CUR-[BMPYRR][NTf<sub>2</sub>]@ncSi nanocapsules which have a lower IL relative composition (as concluded from TGA and EA results). The obtained  $K_L a$  for CUR-IL@ncSi followed the trend: [OMIM][NTf<sub>2</sub>] > [P<sub>6,6,6,14</sub>][NTf<sub>2</sub>] > [BMPYRR][NTf<sub>2</sub>]. It was expected that these values would follow the O<sub>2</sub> solubility trend for these ILs (Table 1); however, as already discussed, the relative IL amounts incorporated into the nanocapsules are quite different for the three studied systems, namely in the case of CUR-[BMPYRR][NTf<sub>2</sub>]@ncSi. The same justification (together with the observed standard deviation values) can explain the trend observed for  $K_L a$  values of CUR-IL/water emulsions: [OMIM][NTf<sub>2</sub>] ≈ [P<sub>6,6,6,14</sub>][NTf<sub>2</sub>] > [BMPYRR][NTf<sub>2</sub>].

### 3.3. Singlet Oxygen Generation

The capacity of curcumin (CUR) to generate <sup>1</sup>O<sub>2</sub> when irradiated with appropriate light was confirmed by the direct detection of the <sup>1</sup>O<sub>2</sub> phosphorescence emission decay, collected at 1275 nm, using samples of CUR dissolved in bulk ILs (CUR-[BMPYRR][NTf<sub>2</sub>], CUR-[OMIM][NTf<sub>2</sub>], and CUR-[P<sub>6,6,6,14</sub>][NTf<sub>2</sub>]) or encapsulated into CUR-IL@ncSi nanocapsules. The time-resolved data (Figure 5) were fitted to an exponential model and the <sup>1</sup>O<sub>2</sub> lifetimes were calculated accordingly. The results are shown in Table 3. The <sup>1</sup>O<sub>2</sub> lifetime in solution strongly depends on its surroundings, namely the solvent [15]. For example, the <sup>1</sup>O<sub>2</sub> lifetime in water is about 3–4 μs while in deuterated water it is 57 μs [15]. The lifetimes of <sup>1</sup>O<sub>2</sub> in the bulk ILs were found to be much higher than in water: 35 μs ([BMPYRR][NTf<sub>2</sub>]), 28 μs ([P<sub>6,6,6,14</sub>][NTf<sub>2</sub>]), and 27 μs ([OMIM][NTf<sub>2</sub>]). In the literature, there are only a few reports concerning the generation of <sup>1</sup>O<sub>2</sub> by PS dissolved in ILs, but two of the already studied ILs are [BMPYRR][NTf<sub>2</sub>] and [OMIM][NTf<sub>2</sub>] [45,46]. The values reported in these works were 44.4 μs, for <sup>1</sup>O<sub>2</sub> generated by rose Bengal dissolved in [BMPYRR][NTf<sub>2</sub>] [45], and 34.5 μs, for <sup>1</sup>O<sub>2</sub> generated by methylene blue dissolved in [OMIM][NTf<sub>2</sub>] [46].

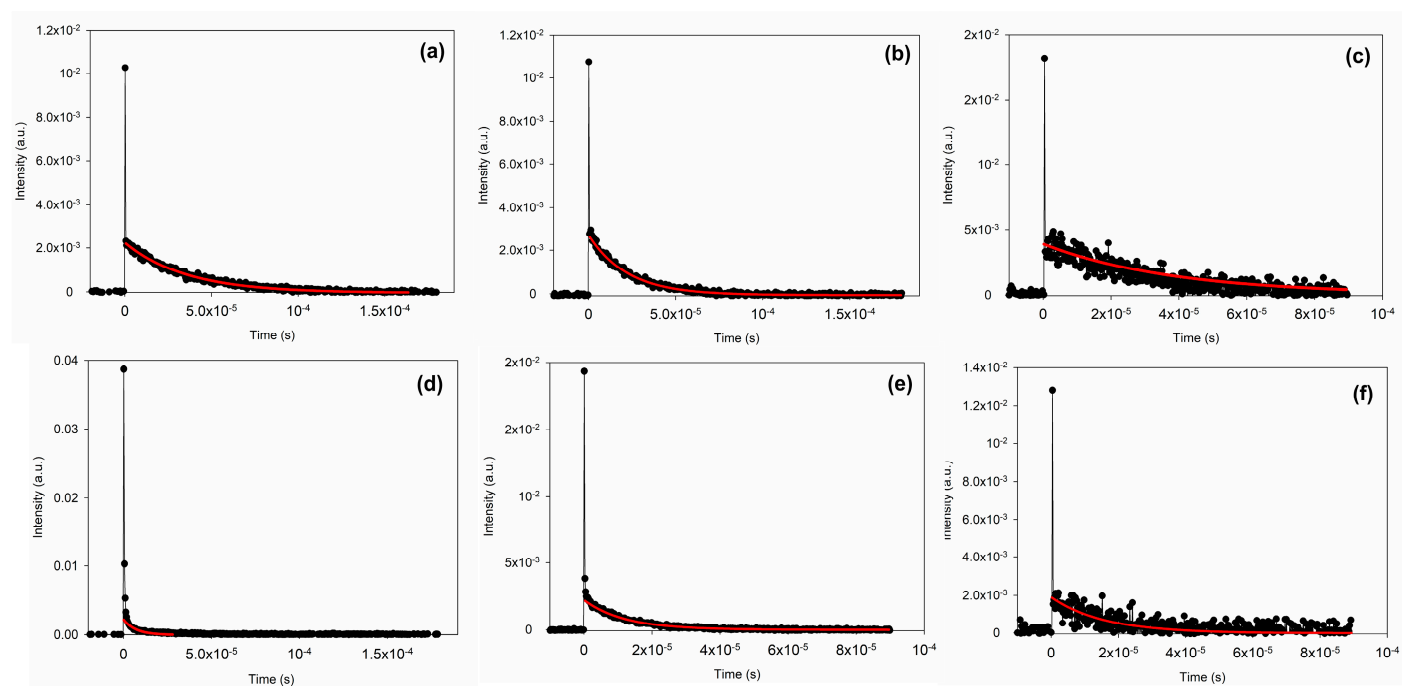


**Figure 5.** Singlet oxygen phosphorescence emission decays collected at 1275 nm after photosensitization with curcumin: (a) CUR-[BMPYRR][NTf<sub>2</sub>]; (b) CUR-[OMIM][NTf<sub>2</sub>]; (c) CUR-[P<sub>6,6,6,14</sub>][NTf<sub>2</sub>]; (d) CUR-[BMPYRR][NTf<sub>2</sub>]@ncSi; (e) CUR-[OMIM][NTf<sub>2</sub>]@ncSi; and (f) CUR-[P<sub>6,6,6,14</sub>][NTf<sub>2</sub>]@ncSi. Note: Due to the highly scattering medium of the solutions/suspensions and although a Newport long band-pass RG1000 filter was used, the initial part of the decays presented a spike that is attributed to scatter light. This feature was not considered in the kinetic analysis of the decays, which were well-fitted with a single-exponential decay law.

**Table 3.** <sup>1</sup>O<sub>2</sub> lifetimes (μs) in the different tested samples.

Sample	[BMPYRR][NTf <sub>2</sub> ]	[OMIM][NTf <sub>2</sub> ]	[P <sub>6,6,6,14</sub> ][NTf <sub>2</sub> ]
CUR-IL solution	35	27	28
CUR-IL@ncSi suspension	4.5	12	16

It was observed that the lifetimes of the <sup>1</sup>O<sub>2</sub> generated in the CUR-IL@ncSi nanocapsule suspension were considerably shorter than the lifetimes of <sup>1</sup>O<sub>2</sub> in the CUR-IL bulk solutions, reflecting the different environments probed by <sup>1</sup>O<sub>2</sub> during its lifetime. Indeed, depending on where <sup>1</sup>O<sub>2</sub> is generated (in the IL core, in the silica shells, or on the surface of CUR-IL@ncSi nanocapsules), these oxygen species will encounter different environments on their diffusion path before decaying, which will be reflected in its phosphorescence emission decay kinetics [47]. The similarity of the <sup>1</sup>O<sub>2</sub> lifetime generated in the [BMPYRR][NTf<sub>2</sub>]@ncSi nanocapsule suspension (4.5 μs) with the lifetime of <sup>1</sup>O<sub>2</sub> in water suggests that the medium in which the <sup>1</sup>O<sub>2</sub> phosphorescence decays is mainly an aqueous environment implying that <sup>1</sup>O<sub>2</sub> is essentially photosensitized in the nanocapsules shells, near to the surface, where it can rapidly diffuse into the aqueous surroundings. This implies that in CUR-[BMPYRR][NTf<sub>2</sub>]@ncSi nanocapsules, CUR is mainly trapped/adsorbed in the silica shells or in IL regions near the silica shell, rather than only in the IL bulk. This means that, despite the very low water solubility of CUR ( $\approx 5.4 \times 10^{-10}$  mol/mol [30]), the relatively higher water solubility of [BMPYRR][NTf<sub>2</sub>] allows CUR to migrate from the core into the silica shell and water, being partially adsorbed on the silica shell by hydrogen bonding and electrostatic interactions between its OH groups and the silanol groups of silica [48]. On the contrary, due to the higher hydrophobicity of the other two ILs, one should expect more favorable interactions between these ILs and the highly hydrophobic CUR molecules. This may lead to their improved ability to retain CUR in their bulk and thus

to the significantly higher  $^1\text{O}_2$  lifetimes observed for the CUR-[OMIM][NTf<sub>2</sub>]*@*ncSi and CUR-[P<sub>6,6,6,14</sub>][NTf<sub>2</sub>]*@*ncSi suspensions (12  $\mu\text{s}$  and 16  $\mu\text{s}$ , respectively). These differences may have some impact on the therapeutic performance of these nanosystems, as  $^1\text{O}_2$  must be released into its surroundings before decaying to the ground state to effectively react with the biological targets. The relationship between the distribution of photosensitizer molecules within a nanoparticle and its ability to release singlet oxygen has been demonstrated by Kabanov et al. (2018) [49]. The authors immobilized three PSs, with distinct degrees of hydrophobicity, in different regions of the mesoporous silica nanoparticles and demonstrated that the nanosystem having the PS distributed mainly on the surface released the major part of the produced  $^1\text{O}_2$  to its surroundings. On the contrary, the nanosystem in which the PS molecules were distributed throughout the depth of the nanoparticles released only a tiny amount of the produced  $^1\text{O}_2$  [49].

The capacity of CUR-IL*@*ncSi nanocapsules to release  $^1\text{O}_2$  into their aqueous vicinity upon irradiation with blue light was probed by an indirect chemical method, using 1,3-diphenylisobenzofuran (DPBF). DPBF reacts irreversibly with singlet oxygen causing a decrease in the intensity of its absorption spectrum around 420 nm. Since DPBF and curcumin have absorption bands in the same region (400–450 nm), the overlap of the two bands makes it more difficult to analyze the results (Figure 6a). In addition, the wavelength of the blue light used (~450 nm), which is close to the absorption maxima of DPBF, can also promote photodegradation. To investigate this effect, DPBF was dissolved in a mixture of EtOH:water (1:9 *v/v*). As shown in Figure 6b, the normalized absorbance at 416 nm of the aerated DPBF solution (with oxygen dissolved at atmospheric pressure) decays faster in the sequentially irradiated solution than in the solution kept in the dark, confirming the occurrence of photobleaching due to irradiation with blue light. However, even for the DPBF solution kept in the dark, it was observed that the absorbance intensity decreased which indicates the high photosensitivity of this molecule. Similar results were observed after irradiation of the DPBF + CUR solution (Figure 6b), indicating that the degradation of DPBF can be attributed mainly to the photobleaching effect rather than the photodynamic one, possibly due to the low  $^1\text{O}_2$  quantum photosensitization efficiency of curcumin in aerated aqueous solutions (about 0.01, according to Chignell et al. [26]).

Figure 6c shows the absorbance spectra of DPBF dissolved in CUR-[BMPYRR][NTf<sub>2</sub>]*@*ncSi suspensions (at equilibrium with air) upon successive irradiation with blue light. The normalized absorbance at 416 nm is plotted in Figure 6d, for irradiated and non-irradiated samples. It can be observed that, like the solution samples, the decrease in absorbance of the irradiated and non-irradiated nanocapsule suspensions is identical, indicating that, under the investigated conditions, the photobleaching of DPBF is the dominant effect rather than the reaction of DPBF with curcumin photosensitized  $^1\text{O}_2$ . Identical results were obtained for CUR-[OMIM][NTf<sub>2</sub>]*@*ncSi and CUR-[P<sub>6,6,6,14</sub>][NTf<sub>2</sub>]*@*ncSi nanocapsule suspensions (Figure 6e,f, respectively).

On the contrary, for oxygen-saturated suspensions (blue plots in Figure 6d–f), a significantly faster absorbance decrease with irradiation time was observed for all three systems. This result can be attributed to the enhancement of  $^1\text{O}_2$  photosensitization by the curcumin incorporated in CUR-IL*@*ncSi nanocapsules due to the increase of oxygen concentration in the vicinity of curcumin molecules. Moreover, it also indicates that the generated  $^1\text{O}_2$  can diffuse to some extent from the nanocapsules to the aqueous surroundings, since the DPBF is in the aqueous phase.

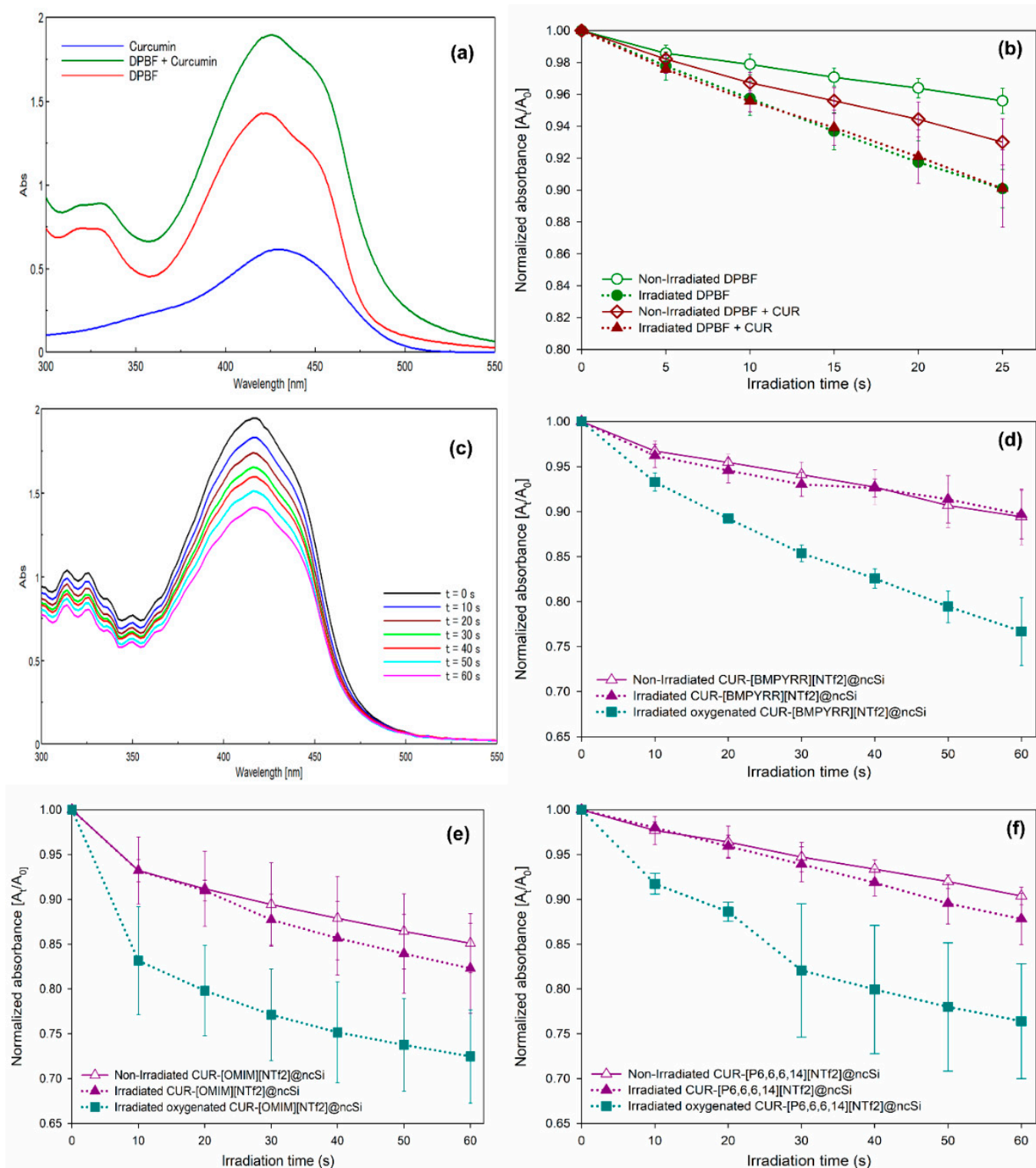


**Figure 6.** Singlet oxygen,  $^1O_2$ , detection by a chemical probe (DPBF) in aerated and oxygen-saturated (oxygenated) solutions or suspensions: (a) UV-VIS absorbance spectrum of DPBF, curcumin, and DPBF + curcumin in EtOH:water solutions (1:9 v/v); (b) normalized absorbance at 416 nm of a DPBF solution (1:9 EtOH:water v/v) and DPBF+curcumin solution (1:9 EtOH:water v/v), in the dark or after successive irradiation with blue light; (c) changes in the absorbance spectrum of DPBF in CUR-[BMPYRR][NTf<sub>2</sub>]@ncSi suspensions upon successive irradiation; (d–f) normalized absorbance at 416 nm of DPBF in CUR-IL@ncSi suspensions (1:9 EtOH:water v/v): in the dark; upon successive irradiation; and upon successive irradiation following oxygenation of the suspensions.

### 3.4. Antimicrobial Photodynamic Effect

The potential antimicrobial photodynamic effect of CUR-IL@ncSi nanocapsules was tested against *L. rhamnosus*, a Gram-positive bacterium, with nanocapsules incorporated into gelatin films (see Figures S7 and S8 in the supplementary material for film photos and micrographs). Films containing CUR-IL@ncSi or IL@ncSi nanocapsules were immersed in bacterial suspensions and irradiated with blue light. A blank control (bacteria only) and a gelatin film (without nanocapsules) were used as controls. After contact and irradiation, bacteria suspensions were inoculated into a culture medium, and their growth was followed over time by measuring the optical density of the cultures at 600 nm [50].

No relevant statistical differences ( $p > 0.05$ ) were observed in bacterial growth after bacteria were incubated with the different films for 30 min in the dark (Figure 7a), indicating that gelatin and nanocapsules per se do not have an acute harmful effect. Similarly, no significant antibacterial effect ( $p > 0.05$ ) was observed in the control group (bacteria only) after exposure to blue light for one or two hours (Figure 7b).

The antibacterial photodynamic effect of the CUR-IL@ncSi nanocapsules was evaluated against IL@ncSi nanocapsules (without CUR) for different irradiation times. As expected, without irradiation (Figure 7c,f,i), no significant statistical differences ( $p > 0.05$ ) were observed between the two groups at different incubation times. After 1 h of irradiation (Figure 7d,g,j), only the CUR-[P<sub>6,6,6,14</sub>][NTf<sub>2</sub>]-@ncSi-loaded film showed significant differences in the OD<sub>600</sub> at 10 and 12 h of incubation, which can be attributed to the photodynamic effect. After two hours of irradiation (Figure 7e,h,k), both CUR-[P<sub>6,6,6,14</sub>][NTf<sub>2</sub>]-@ncSi- and CUR-[BMPYRR][NTf<sub>2</sub>]-@ncSi-loaded films showed significant differences in bacterial growth. These differences were more pronounced for the bacteria exposed to CUR-[BMPYRR][NTf<sub>2</sub>]-@ncSi, which may be a direct consequence of the relatively higher capacity of these nanocapsules to release <sup>1</sup>O<sub>2</sub>, as proposed and discussed previously. As for CUR-[OMIM][NTf<sub>2</sub>]-@ncSi-loaded films, no differences in bacterial growth were observed that could be attributed to the photodynamic effect, for 1 h and 2 h irradiation ( $p > 0.05$ ). However, it is expected that these nanoparticles could exert the photodynamic antimicrobial effect under different experimental conditions, since their ability to generate <sup>1</sup>O<sub>2</sub> upon irradiation has been demonstrated. It should be noted that despite the inhibition of the growth rate, the bacteria still have the capacity to grow, which means that the photodynamic effect caused some damage but did not inactivate the total amount of bacteria.

This test has demonstrated the aPDT effect of CUR-[BMPYRR][NTf<sub>2</sub>]-@ncSi and CUR-[P<sub>6,6,6,14</sub>][NTf<sub>2</sub>]-@ncSi nanoparticles when incorporated into a polymeric support matrix. These results suggest that these nanoparticles can be used to develop biomedical products with antimicrobial capacities (due to their aPDT properties), such as wound dressings for wound infection management [17,18,50]. However, this was only a simple proof-of-concept and a qualitative test, which was performed with non-pathogenic bacteria. Quantitative colony counting tests with model Gram-positive and Gram-negative pathogenic bacteria will be performed in the future.

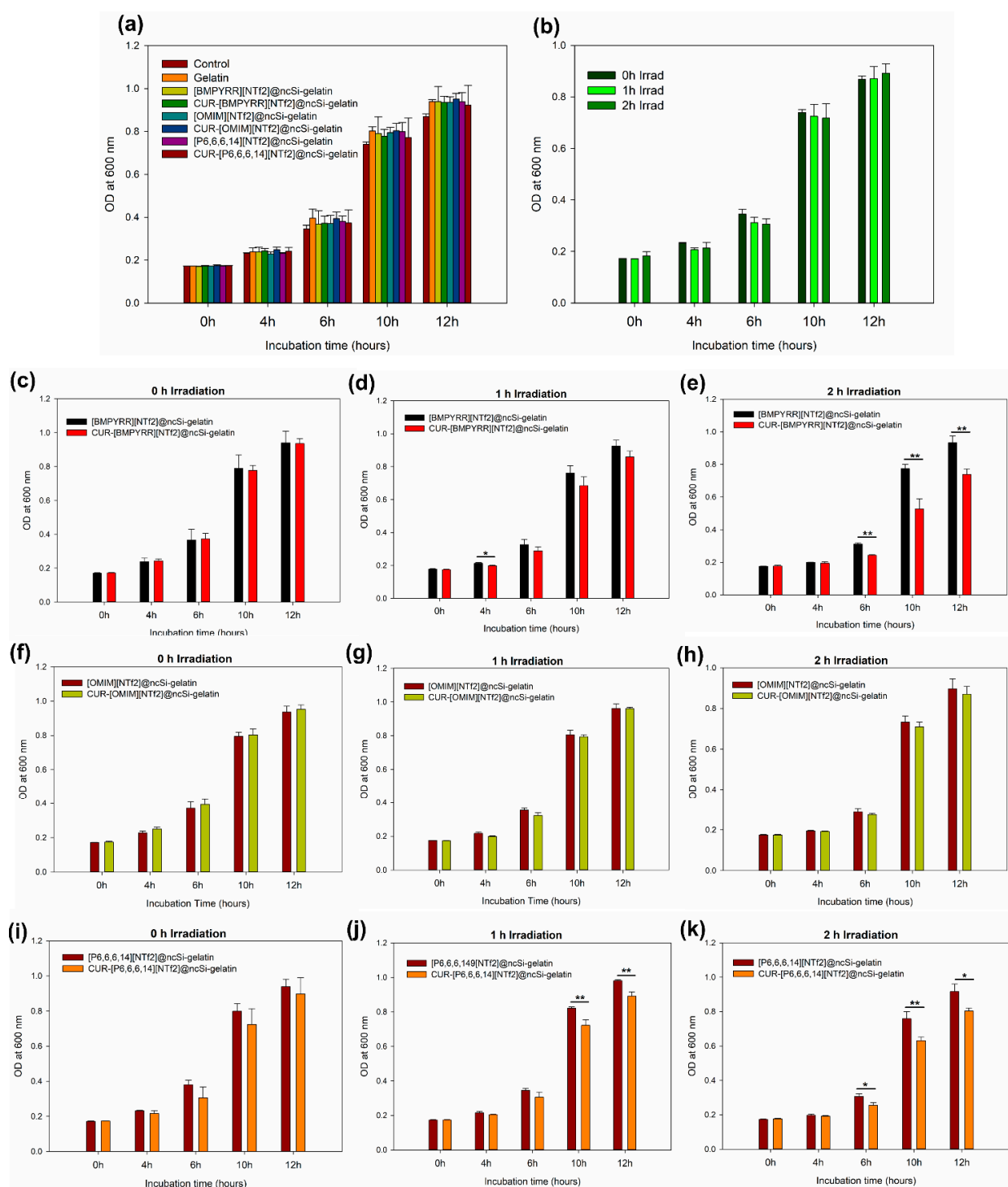


**Figure 7.** Optical density (OD) of *L. rhamnosus* cultures at different incubation times after cells were exposed to different treatments. (a) After 30 min of contact in the dark with the bottom of the culture well (control), gelatin film, gelatin films containing IL@ncSi, and gelatin films containing CUR-IL@ncSi; (b) control group after irradiation with blue light during 0 h, 1 h, or 2 h; (c–e) after contact with [BMPYRR][NTf<sub>2</sub>]@ncS-gelatin film or CUR-[BMPYRR][NTf<sub>2</sub>]@ncSi-gelatin film and irradiation with blue light for 0 h, 1 h, or 2 h; (f–h) after contact with [OMIM][NTf<sub>2</sub>]@ncS-gelatin film or CUR-[OMIM][NTf<sub>2</sub>]@ncSi-gelatin film and irradiation with blue light for 0 h, 1 h, or 2 h; (i–k) after contact with [P<sub>6,6,6,14</sub>][NTf<sub>2</sub>]@ncS-gelatin film or CUR-[P<sub>6,6,6,14</sub>][NTf<sub>2</sub>]@ncSi-gelatin film and irradiation with blue light for 0 h, 1 h, or 2 h. \* p < 0.05; \*\* p < 0.01.

#### 4. Conclusions

Three hydrophobic ILs with dissolved curcumin were successfully encapsulated in silica nanocapsules using a combined original IL-in-water microemulsion/sol-gel method. The ability of the nanocapsules to generate  $^1\text{O}_2$  upon appropriate irradiation was demonstrated by the directed detection of  $^1\text{O}_2$  phosphorescence at 1275 nm. The high oxygen solubility capacities of the encapsulated ILs gave the nanocapsules the ability to dissolve, retain, and release significant amounts of oxygen, as verified by oxygenation/deoxygenation studies. This creates an oxygen-rich environment around CUR molecules that favors the enhancement of  $^1\text{O}_2$  production, as demonstrated by the indirect spectrophotometric method using DPBF as a probe.

Preliminary microbiological tests with CUR-IL@ncSi nanocapsules incorporated into gelatin films showed the occurrence of an antimicrobial effect for CUR-[BMPYRR][NTf<sub>2</sub>]@ncSi and CUR-[P<sub>6,6,6,14</sub>][NTf<sub>2</sub>]@ncSi-loaded gelatin films due to photodynamic inactivation.

Furthermore, the  $^1\text{O}_2$  lifetime for [BMPYRR][NTf<sub>2</sub>]@ncSi nanocapsules was the lowest and identical to the  $^1\text{O}_2$  lifetime in water (~4.0  $\mu\text{s}$ ), suggesting that in this sample  $^1\text{O}_2$  should be mostly photosensitized near the surface of silica shells, and thus CUR should be preferentially distributed on the [BMPYRR][NTf<sub>2</sub>]@ncSi nanocapsules silica shells. The relatively higher water solubility of [BMPYRR][NTf<sub>2</sub>], resulting in the lowest IL content due to partial leaching, could be responsible for the preferential distribution of CUR at the nanocapsules silica shell. Nevertheless, the distribution of curcumin inside the nanocapsules and, consequently, the site of singlet oxygen production and its ability to diffuse to the outside before decaying should be the subject of further studies as this aspect is not clearly elucidated. Future work should also include standard colony courting tests with model Gram-positive and Gram-negative pathogenic bacteria.

This work proves the potential of this new type of nanocapsule for aPDT applications and opens doors for future research, where different photosensitizers and ILs can be tested and the resulting IL@ncSi can be combined with other biomaterials to develop biomedical devices with enhanced oxygenation capacity and aPDT activity.

**Supplementary Materials:** The following supporting information can be downloaded at: <https://www.mdpi.com/article/10.3390/pharmaceutics15041080/s1>. Figure S1: Size distribution of CUR-[BMPYRR][NTf<sub>2</sub>]@ncSi; Figure S2: Size distribution of CUR-[OMIM][NTf<sub>2</sub>]@ncSi; Figure S3: Size distribution of CUR-[P<sub>6,6,6,14</sub>][NTf<sub>2</sub>]@ncSi; Figure S4: Size distribution of the IL droplets in the CUR-[BMPYRR][NTf<sub>2</sub>]/Water emulsion; Figure S5: Size distribution of the IL droplets in the CUR-[OMIM][NTf<sub>2</sub>]/Water emulsion; Figure S6: Size distribution of the IL droplets in the CUR-[P<sub>6,6,6,14</sub>][NTf<sub>2</sub>]/Water emulsion; Figure S7: Gelatin film and gelatin film loaded with CUR-[OMIM][NTf<sub>2</sub>]@ncSi nanocapsules; Figure S8: SEM images of the surface of gelatin films incorporating CUR-IL@ncSi; Table S1: Average hydrodynamic sizes of IL/water emulsions and of the correspondent nanocapsules; Table S2: Maximum concentration of dissolved oxygen ( $p\text{O}_{2\text{Max}}$ ) and the correspondent time ( $t_{\text{Max}}$ ) registered for the different samples. IL/water and NCs/water overall volumetric mass transfer coefficients ( $K_{\text{L}a}$ ).

**Author Contributions:** Conceptualization, H.C.d.S., P.C., M.E.M.B. and A.M.A.D.; methodologies, H.C.d.S., P.C., M.E.M.B., A.M.A.D. and J.P.; formal analysis, J.H., P.C. and J.P.; experimental research, J.H.; resources, H.C.d.S.; writing—original draft preparation, J.H. and P.C.; writing—review and editing, H.C.d.S., J.P., P.C., J.H., A.M.A.D. and M.E.M.B.; visualization, J.H. and P.C.; supervision, H.C.d.S. and P.C.; funding acquisition, H.C.d.S., M.E.M.B. and A.M.A.D. All authors have read and agreed to the published version of the manuscript.

**Funding:** This research was funded by: (i) CIEPQPF-UC (supported by Fundação para a Ciência e a Tecnologia (FCT) through projects UIDB/00102/2020 and UIDP/QUI/00102/2020, co-funded by COMPETE2020-EU); (ii) Fundação Luso-Americana para o Desenvolvimento (Portugal)/National Science Foundation (USA), through Project Ref. A1/Proj. 75/13, FLAD/NSF 2013; (iii) CQC-IMS (supported by FCT through projects UIDB/00313/2020 and UIDP/QUI/00313/2020, co-funded by COMPETE2020-EU); (iv) Laserlab-Europe (no. 284464, EC's 7th Framework Programme). A.M.A.D. acknowledges FCT for a contract under the program Investigador FCT IF/00455/2013 and under the program Stimulus of Scientific Employment—Individual Support, CEECIND/01248/2017.



**Institutional Review Board Statement:** Not applicable.

**Informed Consent Statement:** Not applicable.

**Data Availability Statement:** The data presented in this study are available upon request from the corresponding author.

**Acknowledgments:** Authors acknowledge Susana Alarico, from CNC-UC and CIBB-UC, for providing the bacteria for the antimicrobial photodynamic therapy tests. Authors also wish to acknowledge former students Rui Pinho, Sylvia Sousa, Gustavo Marques, Mariana Silva, and Claudia Buga for their contribution to the development of the nanocapsules' synthesis method and oxygenation/deoxygenation experiments.

**Conflicts of Interest:** The authors declare no conflict of interest.

## References

1. Kwiatkowski, S.; Knap, B.; Przystupski, D.; Saczko, J.; Kędzierska, E.; Knap-Czop, K.; Kotlińska, J.; Michel, O.; Kotowski, K.; Kulbacka, J. Photodynamic therapy—mechanisms, photosensitizers and combinations. *Biomed. Pharmacother.* **2018**, *106*, 1098–1107. [[CrossRef](#)] [[PubMed](#)]
2. Niculescu, A.; Grumezescu, A.; Niculescu, A.; Grumezescu, A. Photodynamic therapy—An up-to-date review. *Appl. Sci.* **2021**, *11*, 3626. [[CrossRef](#)]
3. Xie, J.; Wang, Y.; Choi, W.; Jangili, P.; Ge, Y.; Xu, Y.; Kang, J.; Liu, L.; Zhang, B.; Xie, Z.; et al. Overcoming barriers in photodynamic therapy harnessing nano-formulation strategies. *Chem. Soc. Rev.* **2021**, *50*, 9152–9201. [[CrossRef](#)] [[PubMed](#)]
4. Montaseri, H.; Kruger, C.A.; Abrahamse, H. Inorganic nanoparticles applied for active targeted photodynamic therapy of breast cancer. *Pharmaceutics* **2021**, *13*, 296. [[CrossRef](#)]
5. Hong, E.J.; Choi, D.G.; Shim, M.S. Targeted and effective photodynamic therapy for cancer using functionalized nanomaterials. *Acta Pharm. Sin. B* **2016**, *6*, 297–307. [[CrossRef](#)]
6. Seyyedi Zadeh, E.; Ghanbari, N.; Salehi, Z.; Derakhti, S.; Amoabediny, G.; Akbari, M.; Asadi Tokmedash, M. Smart pH-responsive magnetic graphene quantum dots nanocarriers for anticancer drug delivery of curcumin. *Mater. Chem. Phys.* **2023**, *297*, 127336. [[CrossRef](#)]
7. Moharramnejad, M.; Ehsani, A.; Shahi, M.; Gharanli, S.; Saremi, H.; Malekshah, R.E.; Basmenj, Z.S.; Salmani, S.; Mohammadi, M. MOF as nanoscale drug delivery devices: Synthesis and recent progress in biomedical applications. *J. Drug Deliv. Sci. Technol.* **2023**, *81*, 104285. [[CrossRef](#)]
8. Kim, K.T.; Lee, J.Y.; Kim, D.D.; Yoon, I.S.; Cho, H.J. Recent progress in the development of poly(lactic-co-glycolic acid)-based nanostructures for cancer imaging and therapy. *Pharmaceutics* **2019**, *11*, 280. [[CrossRef](#)]
9. Moghassemi, S.; Dadashzadeh, A.; Azevedo, R.B.; Feron, O.; Amorim, C.A. Photodynamic cancer therapy using liposomes as an advanced vesicular photosensitizer delivery system. *J. Control. Release* **2021**, *339*, 75–90. [[CrossRef](#)]
10. Yu, M.; Xu, X.; Cai, Y.; Zou, L.; Shuai, X. Perfluorohexane-cored nanodroplets for stimulations-responsive ultrasonography and O<sub>2</sub>-potentiated photodynamic therapy. *Biomaterials* **2018**, *175*, 61–71. [[CrossRef](#)]
11. Hu, H.; Yan, X.; Wang, H.; Tanaka, J.; Wang, M.; You, W.; Li, Z. Perfluorocarbon-based O<sub>2</sub> nanocarrier for efficient photodynamic therapy. *J. Mater. Chem. B* **2019**, *7*, 1116–1123. [[CrossRef](#)] [[PubMed](#)]
12. Su, T.; Cheng, F.; Pu, Y.; Cao, J.; Lin, S.; Zhu, G.; He, B. Polymeric micelles amplify tumor oxidative stresses through combining PDT and glutathione depletion for synergistic cancer chemotherapy. *Chem. Eng. J.* **2021**, *411*, 128561. [[CrossRef](#)]
13. Lai, C.; Luo, B.; Shen, J.; Shao, J. Biomedical engineered nanomaterials to alleviate tumor hypoxia for enhanced photodynamic therapy. *Pharmacol. Res.* **2022**, *186*, 106551. [[CrossRef](#)] [[PubMed](#)]
14. Cieplik, F.; Deng, D.; Crielaard, W.; Buchalla, W.; Hellwig, E.; Al-Ahmad, A.; Maisch, T. Antimicrobial photodynamic therapy—what we know and what we don't. *Crit. Rev. Microbiol.* **2018**, *44*, 571–589. [[CrossRef](#)] [[PubMed](#)]
15. Delcanale, P.; Abbruzzetti, S.; Viappiani, C. Photodynamic treatment of pathogens. *Riv. Del Nuovo Cim.* **2022**, *45*, 407–459. [[CrossRef](#)]
16. Awad, M.; Thomas, N.; Barnes, T.J.; Prestidge, C.A. Nanomaterials enabling clinical translation of antimicrobial photodynamic therapy. *J. Control. Release* **2022**, *346*, 300–316. [[CrossRef](#)]
17. Jiang, L.; Loo, S.C.J. Intelligent nanoparticle-based dressings for bacterial wound infections. *ACS Appl. Bio Mater.* **2021**, *4*, 3849–3862. [[CrossRef](#)]
18. Xu, C.; Akakuru, O.U.; Ma, X.; Zheng, J.; Zheng, J.; Wu, A. Nanoparticle-based wound dressing: Recent progress in the detection and therapy of bacterial infections. *Bioconjugate Chem.* **2020**, *31*, 1708–1723. [[CrossRef](#)]
19. Pereira, A.B.; Araújo, J.M.M.; Martinho, S.; Alves, F.; Nunes, S.; Matias, A.; Duarte, C.M.M.; Rebelo, L.P.N.; Marrucho, I.M. Fluorinated ionic liquids: Properties and applications. *ACS Sustain. Chem. Eng.* **2013**, *1*, 427–439. [[CrossRef](#)]
20. Song, T.; Morales-Collazo, O.; Brennecke, J.F. Solubility and diffusivity of oxygen in ionic liquids. *J. Chem. Eng. Data* **2019**, *64*, 4956–4967. [[CrossRef](#)]
21. Wenny, M.B.; Molinari, N.; Slavney, A.H.; Thapa, S.; Lee, B.; Kozinsky, B.; Mason, J.A. Understanding relationships between free volume and oxygen absorption in ionic liquids. *J. Phys. Chem. B* **2022**, *126*, 1268–1274. [[CrossRef](#)] [[PubMed](#)]

22. Akhter, F.; Rao, A.A.; Abbasi, M.N.; Wahocho, S.A.; Mallah, M.A.; Anees-ur-Rehman, H.; Chandio, Z.A. A comprehensive review of synthesis, applications and future prospects for silica nanoparticles (SNPs). *Silicon* **2022**, *14*, 8295–8310. [[CrossRef](#)]
23. Zhang, Y.; Hsu, B.Y.W.; Ren, C.; Li, X.; Wang, J. Silica-based nanocapsules: Synthesis, structure control and biomedical applications. *Chem. Soc. Rev.* **2015**, *44*, 315–335. [[CrossRef](#)] [[PubMed](#)]
24. Dias, L.D.; Blanco, K.C.; Mfouo-Tynga, I.S.; Inada, N.M.; Bagnato, V.S. Curcumin as a photosensitizer: From molecular structure to recent advances in antimicrobial photodynamic therapy. *J. Photochem. Photobiol. C Photochem. Rev.* **2020**, *45*, 100384. [[CrossRef](#)]
25. Yixuan, L.; Qaria, M.A.; Sivasamy, S.; Jianzhong, S.; Daochen, Z. Curcumin production and bioavailability: A comprehensive review of curcumin extraction, synthesis, biotransformation and delivery systems. *Ind. Crop Prod.* **2021**, *172*, 114050. [[CrossRef](#)]
26. Chignell, C.F.; Bilskj, P.; Reszka, K.J.; Motten, A.G.; Sik, R.H.; Dahl, T.A. Spectral and photochemical properties of curcumin. *Photochem. Photobiol.* **1994**, *59*, 295–302. [[CrossRef](#)]
27. Patel, H.S.; Shaikh, S.J.; Ray, D.; Aswal, V.K.; Vaidya, F.; Pathak, C.; Varade, D.; Rahdar, A.; Sharma, R.K. Structural transitions in mixed phosphatidylcholine/pluronic micellar systems and their in vitro therapeutic evaluation for poorly water-soluble drug. *J. Mol. Liq.* **2022**, *364*, 120003. [[CrossRef](#)]
28. Pourmadadi, M.; Abbasi, P.; Eshaghi, M.M.; Bakhshi, A.; Ezra Manicum, A.-L.; Rahdar, A.; Pandey, S.; Jadoun, S.; Díez-Pascual, A.M. Curcumin delivery and co-delivery based on nanomaterials as an effective approach for cancer therapy. *J. Drug Deliv. Sci. Technol.* **2022**, *78*, 103982. [[CrossRef](#)]
29. Li, J.; Wang, Z.; Yao, S.; Song, H. Aqueous solubilization and extraction of curcumin enhanced by imidazolium, quaternary ammonium, and tropine ionic liquids, and insight of ionic liquids-curcumin interaction. *J. Mol. Liq.* **2020**, *317*, 113906. [[CrossRef](#)]
30. Wikene, K.O.; Bruzell, E.; Tønnesen, H.H. Characterization and antimicrobial phototoxicity of curcumin dissolved in natural deep eutectic solvents. *Eur. J. Pharm. Sci.* **2015**, *80*, 26–32. [[CrossRef](#)]
31. Correia, D.M.; Fernandes, L.C.; Fernandes, M.M.; Hermenegildo, B.; Meira, R.M.; Ribeiro, C.; Ribeiro, S.; Reguera, J.; Lanceros-Méndez, S. Ionic liquid-based materials for biomedical applications. *Nanomaterials* **2021**, *11*, 2401. [[CrossRef](#)]
32. Zhuang, W.; Hachem, K.; Bokov, D.; Javed Ansari, M.; Taghvaie Nakhjiri, A. Ionic liquids in pharmaceutical industry: A systematic review on applications and future perspectives. *J. Mol. Liq.* **2022**, *349*, 118145. [[CrossRef](#)]
33. Yan, J.; Mangolini, F. Engineering encapsulated ionic liquids for next-generation applications. *RSC Adv.* **2021**, *11*, 36273–36288. [[CrossRef](#)] [[PubMed](#)]
34. Lambert, E.; Janjic, J.M. Quality by design approach identifies critical parameters driving oxygen delivery performance in vitro for perfluorocarbon based artificial oxygen carriers. *Sci. Rep.* **2021**, *11*, 5569. [[CrossRef](#)] [[PubMed](#)]
35. Seixas de Melo, J.S.; Pina, J.; Dias, F.B.; Maçanita, A.L. Experimental techniques for excited state characterisation. In *Applied Photochemistry*; Evans, R.C., Douglas, P., Burrow, H.D., Eds.; Springer Netherlands: Dordrecht, The Netherlands, 2013; pp. 533–585.
36. Entradas, T.; Waldron, S.; Volk, M. The detection sensitivity of commonly used singlet oxygen probes in aqueous environments. *J. Photochem. Photobiol. B Biol.* **2020**, *204*, 111787. [[CrossRef](#)] [[PubMed](#)]
37. Freire, M.G.; Santos, L.M.N.B.F.; Fernandes, A.M.; Coutinho, J.A.P.; Marrucho, I.M. An overview of the mutual solubilities of water–imidazolium-based ionic liquids systems. *Fluid Phase Equilibria* **2007**, *261*, 449–454. [[CrossRef](#)]
38. Freire, M.G.; Neves, C.M.S.S.; Ventura, S.P.M.; Pratas, M.J.; Marrucho, I.M.; Oliveira, J.; Coutinho, J.A.P.; Fernandes, A.M. Solubility of non-aromatic ionic liquids in water and correlation using a QSPR approach. *Fluid Phase Equilibria* **2010**, *294*, 234–240. [[CrossRef](#)]
39. Freire, M.G.; Carvalho, P.J.; Gardas, R.L.; Santos, L.M.N.B.F.; Marrucho, I.M.; Coutinho, J.A.P. Solubility of Water in Tetradecyltriethylphosphonium-Based Ionic Liquids. *J. Chem. Eng. Data* **2008**, *53*, 2378–2382. [[CrossRef](#)]
40. Neale, A.R.; Li, P.; Jacquemin, J.; Goodrich, P.; Ball, S.C.; Compton, R.G.; Hardacre, C. Effect of cation structure on the oxygen solubility and diffusivity in a range of bis((trifluoromethyl)sulfonyl)imide anion based ionic liquids for lithium–air battery electrolytes. *Phys. Chem. Chem. Phys.* **2016**, *18*, 11251–11262. [[CrossRef](#)]
41. Buzzeo, M.C.; Hardacre, C.; Compton, R.G. Use of room temperature ionic liquids in gas sensor design. *Anal. Chem.* **2004**, *76*, 4583–4588. [[CrossRef](#)]
42. Evans, R.G.; Klymenko, O.V.; Saddoughi, S.A.; Hardacre, C.; Compton, R.G. Electroreduction of oxygen in a series of room temperature ionic liquids composed of group 15-centered cations and anions. *J. Phys. Chem. B* **2004**, *108*, 7878–7886. [[CrossRef](#)]
43. Weiss, E.; Dutta, B.; Kirschning, A.; Abu-Reziq, R. BMIm-PF6@SiO2 Microcapsules: Particulated Ionic Liquid as A New Material for the Heterogenization of Catalysts. *Chem. Mater.* **2014**, *26*, 4781–4787. [[CrossRef](#)]
44. Xing, W.; Yin, M.; Lv, Q.; Hu, Y.; Liu, C.; Zhang, J. Oxygen solubility, diffusion coefficient, and solution viscosity. In *Rotating Electrode Methods and Oxygen Reduction Electrocatalysts*; Xing, W., Yin, G., Zhang, J., Eds.; Elsevier: Amsterdam, The Netherlands, 2014; pp. 1–31.
45. Liu, L.; Zhang, Z.; Zhao, Q.; Chen, X.; Deng, L.; Chen, W.; Jin, Y. Detection of singlet oxygen by chemical trap in ionic liquids. *Chem. Phys. Lett.* **2020**, *739*, 136952. [[CrossRef](#)]
46. Yoshida, T.; Kawai, A.; Khara, D.C.; Samanta, A. Temporal behavior of the singlet molecular oxygen emission in imidazolium and morpholinium ionic liquids and its implications. *J. Phys. Chem. B* **2015**, *119*, 6696–6702. [[CrossRef](#)] [[PubMed](#)]
47. Kabanov, V.; Ghosh, S.; Lovell, J.F.; Heyne, B. Singlet oxygen partition between the outer-, inner- and membrane-phases of photo/chemotherapeutic liposomes. *Phys. Chem. Chem. Phys.* **2019**, *21*, 25054–25064. [[CrossRef](#)]

48. Kim, S.; Stébé, M.-J.; Blin, J.-L.; Pasc, A. pH-controlled delivery of curcumin from a compartmentalized solid lipid nanoparticle@mesostructured silica matrix. *J. Mater. Chem. B* **2014**, *2*, 7910–7917. [[CrossRef](#)] [[PubMed](#)]
49. Kabanov, V.; Press, D.J.; Huynh, R.P.S.; Shimizu, G.K.H.; Heyne, B. Assessment of encapsulated dyes' distribution in silica nanoparticles and their ability to release useful singlet oxygen. *Chem. Commun.* **2018**, *54*, 6320–6323. [[CrossRef](#)]
50. Sun, L.; Song, L.; Zhang, X.; Zhou, R.; Yin, J.; Luan, S. Poly( $\gamma$ -glutamic acid)-based electrospun nanofibrous mats with photodynamic therapy for effectively combating wound infection. *Mater. Sci. Eng. C* **2020**, *113*, 110936. [[CrossRef](#)]

**Disclaimer/Publisher's Note:** The statements, opinions and data contained in all publications are solely those of the individual author(s) and contributor(s) and not of MDPI and/or the editor(s). MDPI and/or the editor(s) disclaim responsibility for any injury to people or property resulting from any ideas, methods, instructions or products referred to in the content.